Dispersion of windborne debris

Peter Richards [a]

[a]*University of Auckland, Auckland, New Zealand, pj.richards@auckland.ac.nz*

1 INTRODUCTION

The damage caused by windborne debris is a complex function of the wind conditions, the availability of debris, the point of release, the aerodynamic characteristics of the debris, the impact dynamics and the strength of the structure impacted. This paper will primarily focus on the aerodynamic and dynamic aspects of this problem and investigate how these affect the dispersion. Lin and Vanmarcke (2010), Holmes et al (2010) and Wehner et al (2010) all propose methods for analyzing or predicting the damage caused by windborne debris. These models generally include some method of calculating the likely trajectory of a single piece of debris and then use a bivariate Gaussian distribution to allow for the scatter or dispersion of impact locations around the calculated point. This paper will consider the likely size and shape of that dispersion.

2 EXPERIMENTAL OBSERVATIONS

2.1 *Tachikawa's experiments*

Tachikawa (1988) reports wind tunnel experiments where a range of small plates and square prisms with aspect ratios of 1, 2 and 4 were released with various orientations into an 8.5 m/s airstream and the impact location against a net 0.75 m downstream recorded by video camera. He notes that the distribution of impact locations was "nearly circular and the diameter, which is larger for flat plates than the prisms, increases with the increase in the aspect ratio". The radii of the circles that Tachikawa drew around his scatter plots are given in Table 1.

Table 1. Radii (m) of circles drawn by Tachikawa (1988)

Aspect Ratio L_X/L_Y	1	2	4
Plates $L_Z/L_Y = 0.056$	0.25	0.29	0.31
Square Prism $L_Z/L_Y = 1.0$	0.15	0.20	0.25

The notation used throughout this paper has the dimensions ranked in the order $L_X \geq L_Y \geq L_Z$, and so the aspect ratio is L_X/L_Y and the thickness ratio L_Z/L_Y. In addition the terminology, proposed by Wills et al (2002), which differentiates between compact debris (with all three dimensions of similar size), sheets or plates (with one dimension much smaller than the other two) and rods (with one dimension much bigger than the others) will be used.

It may be noted from Table 1 that the smallest dispersion occurred with a cube (square prism with aspect ratio =1). This occurs because all faces are of equal area and so with most orientations the pressures acting on one face are balanced in the cross flow direction by the pressures on the opposite face. There is however a difference front to rear and so the dominant force is simply a drag force. The flight of compact debris is discussed in detail by Holmes (2004) and will not be considered further in this paper.

The general trend in Table 1 is for increased dispersion as the ratio of the largest to the smallest dimension increases, however this is obviously not a linear relationship since the radii for the aspect ratio 1 plate is the same as that for the aspect ratio 4 square prism.
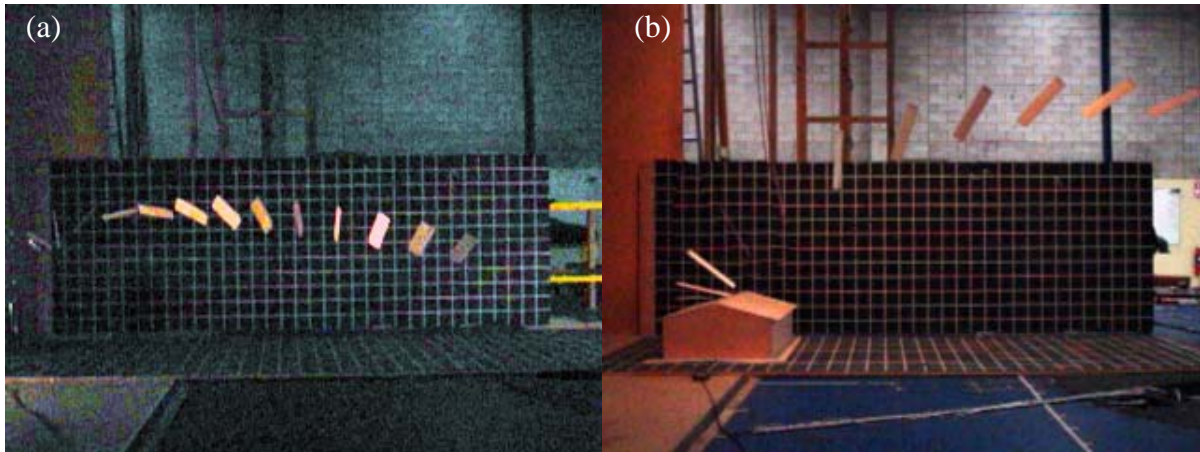
Figure 1. Multiple exposure photography of plate type debris in the University of Auckland wind tunnel, (a) released in uniform flow and (b) released from a model garage.

2.2 University of Auckland experiments

Experiments in the University of Auckland open jet wind tunnel have used two Sony P200 cameras in burst mode to record 16 images, from two orthogonal directions, of the motion of $1/10^{th}$ scale models of sheet and rod type debris. Initially sheets with aspect ratios of 1 and 2 were released into a 9.5 m/s wind-stream from a stand mounted electro-magnet. Figure 1(a) shows an example of the ensemble side view image, a similar image was simultaneous obtained from above the flight path. A variety of release orientations were used. The location of the object at each stage was estimated from the image and parallax corrections made by using the other image to indicate how far the object was from the backboard. In later testing a 4.5 aspect ratio sheet was released from the roof of a model garage. On initial testing it was found that the plate left the field of view and so the tunnel speed was reduced to 6.5 m/s, which reduced the maximum height of flight to about two thirds of that in the higher wind.

Figure 2 shows a collection of trajectories obtained with aspect ratio 2 plates when released with a variety of orientations. These trajectories show that the most significant dispersion occurs during the very early stages of the flight with most of them following almost parallel paths after the initial 300 mm of downstream distance. This initial rapid dispersion occurs due to two main factors: First at this stage the plates are moving relatively slowly and so the relative velocity is maximized and hence the aerodynamic forces are high and secondly the plates are only rotating slowly and so a force may act in one direction for a long period.
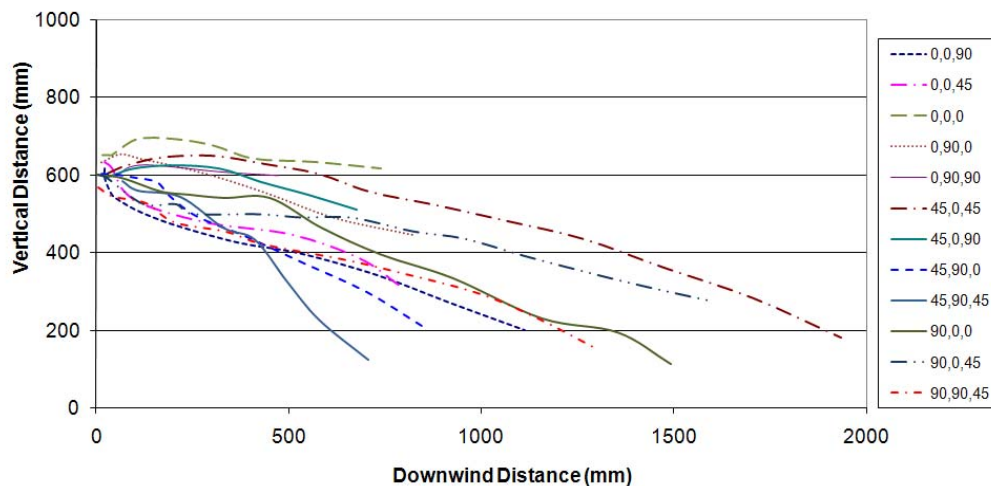

Figure 2. Observed side view trajectories of aspect ratio 2 plates in a 9.5 m/s wind.

Figure 1(b) illustrates a number of other factors which in practice may affect dispersion. These include the non-uniform flow field around a building, which may help to lift a piece of debris to heights that wouldn't occur in a uniform horizontal flow or alternatively create a dead region where the debris will rapidly fall to the ground, and the slower rotation of a high aspect ratio plate which can then gain lift or side force for an extended period.

3   COMPUTATIONAL OBSERVATIONS

Richards et al (2008) computed the trajectories of 2.25 m^2 plates with a mass of 8.1 kg and aspect ratios of 1, 2 and 4 in a 30 m/s wind. As with the experimental tests the initial orientations were varied. Data was presented for an impact 50 m downstream. The results were similar to those obtained by Tachikawa (1988) in as far as the dispersion patterns were almost circular and the standard deviation of transverse locations increased from 7.3 m with a square plate to about 9 m for the other aspect ratios. The standard deviations of vertical locations also changed in this manner.

Figure 3 shows details of the trajectories computed for the square plate. It may be observed that the most significant dispersion occurs during the first 10 m with only a gradual spread in the paths beyond 30 m. Further the velocities in Figures 3(c) and 3(d) show that in almost all cases the highest cross-flow velocities occur in the first few metres of the flight with a gradual decrease thereafter. For the horizontal transverse velocity these tend to decrease towards a small value while the vertical velocities converge to a steady downward velocity under the influence of gravity. Further inspection of these results shows that these high cross-flow accelerations occur during the initial rotation of the plate from its initial angle of attack relative to the flow up to the point where it is almost perpendicular. This behaviour suggests that the trajectories might be modelled as a two stage process, a first stage where rotation and transverse forces need to be considered and a second stage where considering only the mean drag might be sufficient.
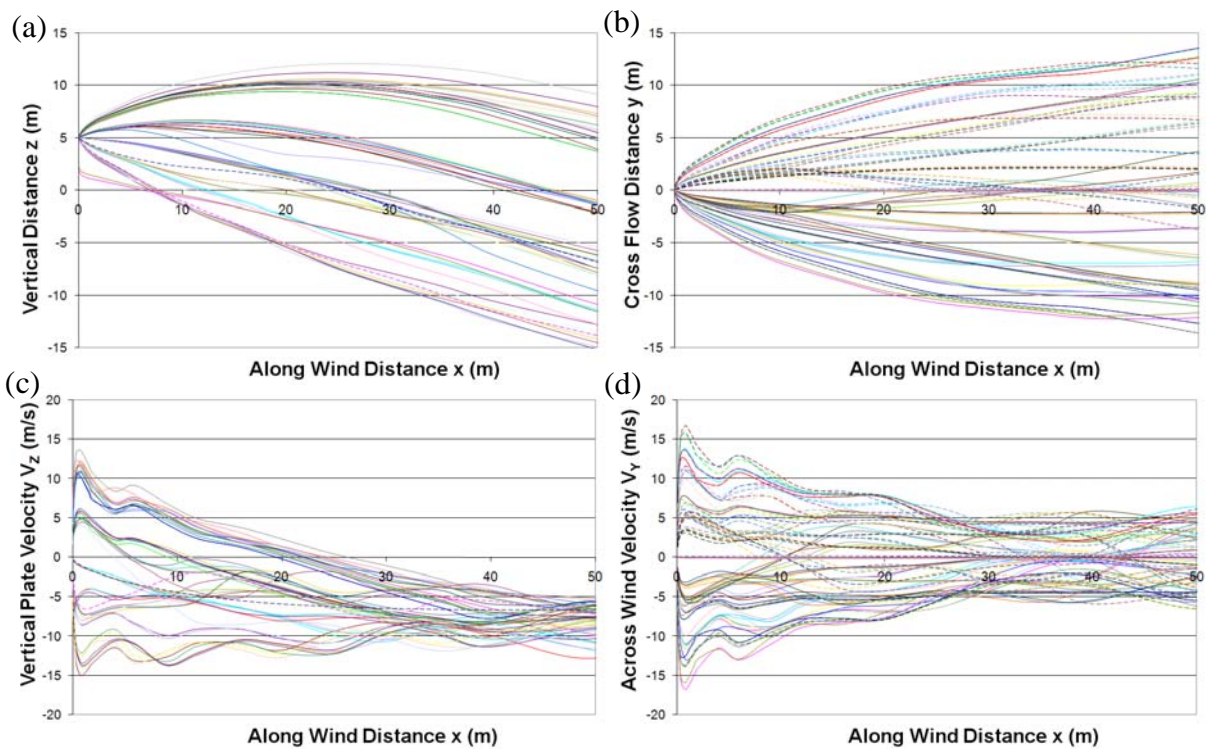

Figure 3. Computed trajectories of 1.5 m square plates in a 30 m/s wind: (a), (b) vertical and transverse locations and (c), (d) velocities.

4 APPROXIMATE TRAJECTORY ANALYSIS

With the numerical results presented in section 3 it is difficult to fully appreciate the influence of the various factors which may affect dispersion. However by making a number of approximations some useful results can be obtained.

4.1 *Initial phase motion*

For both rod and plate type debris there appears to be an initial phase of a trajectory where the across wind (transverse) accelerations are very high. These accelerations are at their highest when the largest face, of area $A_Z = L_X$ x L_Y, is exposed to the wind, in which case the dominant force is the normal force on that face and the dominant moment that caused by the normal force about the y-axis. In such cases the normal force and the associated moment may be assumed to be functions of the angle of attack (α-θ) between the relative velocity (U) and the largest face as illustrated in Figure 4. Martinez-Vazquez et al. (2010) have shown that once the object starts to rotate significantly the forces and moments will also depend on the rate of rotation, but in the initial phase the rates of rotation are gradually increasing from zero and so it seems reasonable to ignore such effects. In this initial phase analysis the axial direction is aligned with the wind while the transverse direction is perpendicular to the wind and in the plane containing the largest dimension of the object. It may be noted that the transverse direction could be any crosswind direction, up, down, horizontal or anywhere in between.
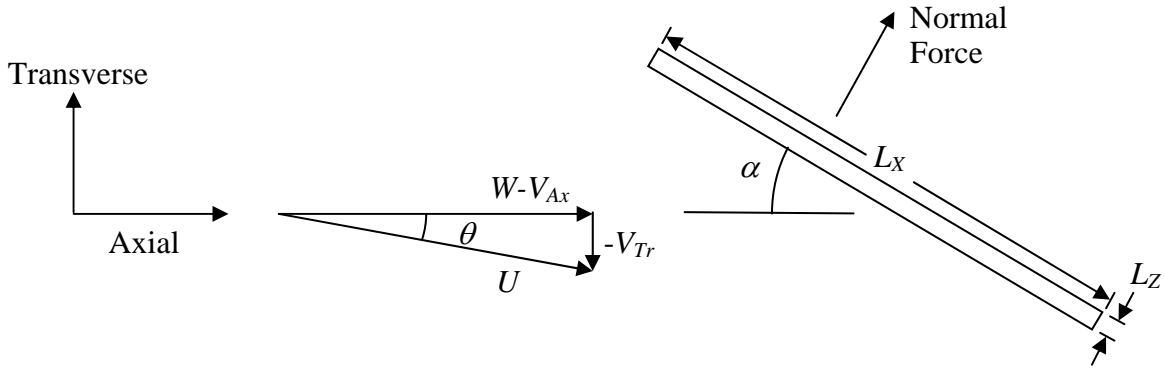

Figure 4. General geometry used in the initial phase analysis.

The basic equations of motion for this situation are:

$$m\frac{dV_{Ax}}{dt} = m\frac{d^2 x_{Ax}}{dt^2} = C_N(\alpha - \theta)\frac{1}{2}\rho_{Air}U^2 A_Z \sin(\alpha) \tag{1}$$

$$m\frac{dV_{Tr}}{dt} = m\frac{d^2 x_{Tr}}{dt} = C_N(\alpha - \theta)\frac{1}{2}\rho_{Air}U^2 A_Z \cos(\alpha) \tag{2}$$

$$I_{YY}\frac{d\omega_Y}{dt} = I_{YY}\frac{d^2\alpha}{dt^2} = C_M(\alpha - \theta)\frac{1}{2}\rho_{Air}U^2 A_Z L_X \tag{3}$$

where $\tan(\theta) = (V_{Tr})/(W-V_{Ax})$ and $U^2 = (W-V_{Ax})^2 + (-V_{Tr})^2$.

In order to integrate these equations it is necessary to define the relationships between the normal force and moment coefficients and the angle of attack (α-θ). Figure 5 shows a range of force and moment coefficients measured in the University of Auckland Wind Tunnel. The three plates had a thickness of 7 mm and a largest face area of 0.25 m^2, but had aspect ratios of '1 to 1' (0.5 m x 0.5 m), '2 to 1' (0.707 m x 0.3535 m) and '4 to 1' (1 m x 0.25 m). The two rods shown here had a length of 1.5 m, nominal thickness of 50 mm but had widths of 100 mm and 150 mm for the '2 to 1' and '3 to 1' rods respectively.
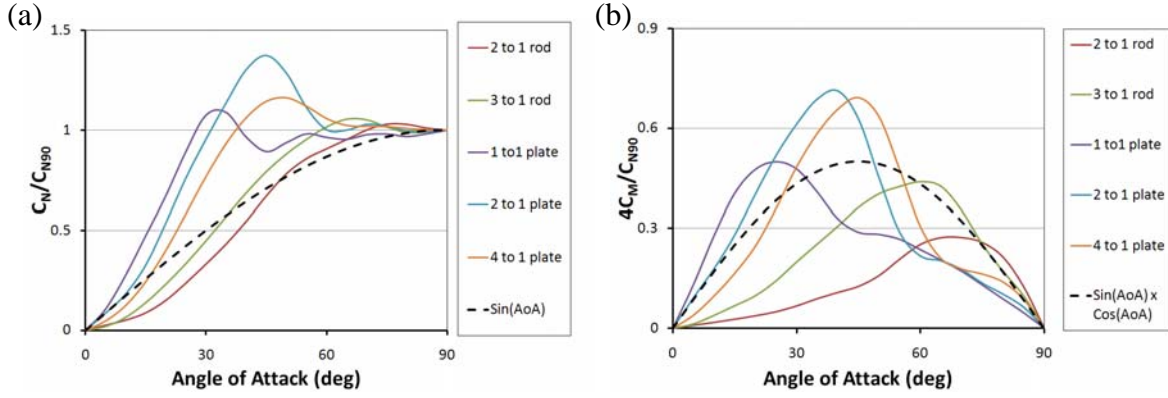
Figure 5. Wind tunnel data for (a) normal force coefficient and (b) moment coefficient for three plate and two rod geometries.

In Figure 5 the normal force coefficient has been normalised by dividing by its value at 90° (C_{N90}) and the moment coefficient normalised by dividing by C_{N90} and by 0.25, which reflects the expectation that at low angles the centre of pressure will be about one quarter of the chordwise length to windward of the centre. With all of these geometries the normalised normal force variation with angle of attack can be crudely approximated as a sine function and similarly the normalised moment coefficient approximated as sine times cosine, although this is a particularly poor approximation for the '2 to 1' rod.

The major approximations, limitations and assumptions used in analysing the initial phase are as follows:

- The object is rectangular with $L_X >> L_Z$ and hence $I_{YY} \approx m L_X^2/12$.
- The intermediate length L_Y is initially perpendicular to the wind.
- The relative wind speed remains close to the wind speed ($U \approx W$).
- The transverse velocities remain small in comparison with the wind speed ($V_{Tr} << W$) and as a result θ is small and hence the angle of attack $\alpha - \theta \approx \alpha$.
- The normal force coefficient for the largest face increases from zero at zero angle of attack ($\alpha = 0°$) to a maximum C_{N90} when $\alpha = 90°$ such that $C_N(\alpha) = C_{N90} \sin(\alpha)$.
- The centre of pressure moves from $L_X/4$ windward of the face centre at $\alpha = 0°$ to the centre at $\alpha = 90°$ in proportion to $\cos(\alpha)$ and hence $C_M(\alpha) = C_{N90}\sin(\alpha)\cos(\alpha)/4$.
- The object has uniform density and hence $m = \rho_{Solid} L_X L_Y L_Z$.

With these approximations some of the equations of motion can be directly integrated between the initial angle $\alpha = \alpha_0$ and $\alpha = \pi/2$ rad = 90° at the end of the initial phase, giving:

$$\omega_{Y1} = \frac{W}{L_X}\left(\frac{3C_{N90}\rho_{air}L_X}{2\rho_{Solid}L_Z}\right)^{0.5}(1-\sin^2\alpha_0)^{0.5} \tag{4}$$

$$V_{Tr1} = \frac{L_X}{3}\omega_{Y1} = W\left(\frac{C_{N90}\rho_{Air}L_X}{6\rho_{Solid}L_Z}\right)^{0.5}(1-\sin^2\alpha_0)^{0.5} \tag{5}$$

$$x_{Tr1} = \frac{L_X}{3}(\pi/2 - \alpha_0) \tag{6}$$

where it has been assumed that the object is initially at rest and at the origin.

It may be noted that the transverse velocity, which is the primary driver for dispersion, is proportional to the wind speed and to the square-root of the 90° normal force coefficient C_{N90}, the air to solid density ratio and the length ratio L_X/L_Z (which is equal to the product of the aspect ratio L_X/L_Y and the thickness ratio L_Y/L_Z). The proportionality to the wind speed matches the wind tunnel observation of reduced flight height with lower wind speed, as men-

tioned in Section 2.2, while the latter result is consistent with the observations made by Tachikawa (1988) and Richards et al (2008) regarding dispersion increasing with aspect ratio. The transverse velocity is also larger if α_0 is small. In contrast the transverse displacement only depends on the length of the object and the initial angle, which if small gives $x_{Tr} \approx L_X/2$. Equations 4-6 could also be used if the plate or rod was initially oriented with the longest length across the flow, once L_X is replaced by L_Y, but both the transverse velocity and displacement would be reduced, which justifies considering the case where the longest dimension is aligned with the flow.

While Equations 4-6 can be derived exactly from the simplified equations of motion, other results require the solution of more complex integrals such as

$$V_{Ax1} = W \left(\frac{C_{N90} \rho_{Air} L_X}{6 \rho_{Solid} L_z} \right)^{0.5} \int_{\alpha_0}^{\pi/2} \frac{\sin^2(\alpha)}{\left(\sin^2(\alpha) - \sin^2(\alpha_0) \right)^{0.5}} d\alpha \tag{7}$$

for which there is no simple expression. As a result numerical integration has been carried out and the results fitted with simple expressions, all of which are accurate to ±2%. This approach has yielded the following addition results for the end of the initial phase:

$$t_1 \approx \frac{L_X}{W} \left(\frac{2 \rho_{Solid} L_Z}{3 C_{N90} \rho_{air} L_X} \right)^{0.5} (1.537 - 0.933 \ln(\sin(\alpha_0))) \tag{8}$$

$$V_{Ax1} \approx W \left(\frac{C_{N90} \rho_{air} L_X}{6 \rho_{Solid} L_Z} \right)^{0.5} (1.0 + 0.174 \sin(\alpha_0) + 0.633 \sin^2(\alpha_0) - 0.234 \sin^3(\alpha_0)) \tag{9}$$

$$x_{Ax1} \approx \frac{L_X}{3} (0.671 + 0.577 \sin(\alpha_0)) \tag{10}$$

If the initial angle of attack is small then the axial velocity is approximately equal to the transverse velocity and the axial displacement is approximately $L_X/4$.

4.2 Second phase motion

Following the initial violent accelerations there is a second phase where more gradual processes take place and the trajectory may be modelled as that of a compact object. The only significant force is the drag, which is characterised by a mean drag coefficient C_D. In this phase the analysis is carried out in three dimensional space as illustrated in Figure 6, with the x-axis aligned with the mean wind and the z-axis vertical. The primary approximations made for this phase are:

- Both the y and z direction velocities are small in comparison with the x direction relative velocity $(W-V_X)$, with the result that $|U| \approx |(W-V_X)|$.
- The reference area used for drag calculations is the largest face area, $A_{REF} = L_Z \times L_Y$.
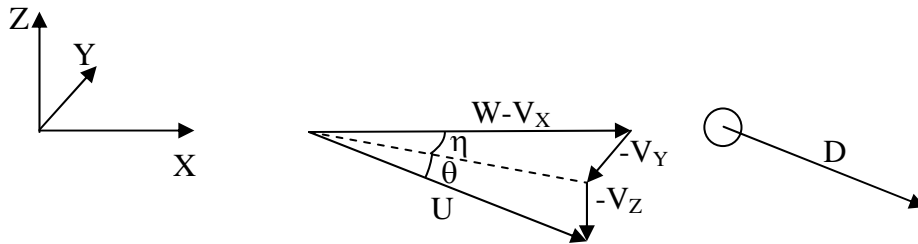- The drag force is aligned with the relative velocity vector **U**.

Figure 6. General geometry used in the second phase analysis.

For this phase the basic equations of motion are:

$$m\frac{dV_X}{dt} = C_D \frac{1}{2} \rho_{Air} U^2 A_{REF} \cos(\theta)\cos(\eta) \tag{11}$$

$$m\frac{dV_Y}{dt} = -C_D \frac{1}{2} \rho_{Air} U^2 A_{REF} \cos(\theta)\sin(\eta) \tag{12}$$

$$m\frac{dV_Z}{dt} = -C_D \frac{1}{2} \rho_{Air} U^2 A_{REF} \sin(\theta) - mg \tag{13}$$

where $U^2=(W-V_X)^2 + (-V_Y)^2 + (-V_Z)^2$. Also from Figure 6, $\sin(\theta)=V_Z/U$, $\cos(\theta)\sin(\eta)=V_Y/U$ and $\cos(\theta)\cos(\eta)=(W-V_X)/U$, so Equations 11-13 can be rewritten as:

$$\frac{dV_X}{dt} = B|W-V_X|(W-V_X) \tag{14}$$

$$\frac{dV_Y}{dt} = -B|W-V_X|V_Y \tag{15}$$

$$\frac{dV_Z}{dt} = -B|W-V_X|V_Z - g \tag{16}$$

where $B=C_D \rho_{Air} A_{REF}/2m$ is the ballistic coefficient. Integration of these equations leads to:

$$x = x_1 + W(t-t_1) - \frac{1}{B}\ln\left(1+B(W-V_{X1})(t-t_1)\right) \tag{17}$$

$$y = y_1 + V_{Y1}\frac{\ln\left(1+B(W-V_{X1})(t-t_1)\right)}{B(W-V_{X1})} \tag{18}$$

$$z = z_1 + V_{Z1}\frac{\ln\left(1+B(W-V_{X1})(t-t_1)\right)}{B(W-V_{X1})} - g\left(\frac{t}{2B(W-V_{X1})} + \frac{t^2}{4} - \frac{\ln\left(1+B(W-V_{X1})t\right)}{2B^2(W-V_{X1})^2}\right) \tag{19}$$

Equation 19 has three terms, the first two are related to the displacement and velocity at the end of the initial phase, while the third term is purely due to gravity and is independent of the initial phase results. It should be noted that if the plane depicted in Figure 4 is at an angle β to the horizontal plane then $y_1=x_{Tr1}\cos(\beta)$, $V_{Y1}=V_{Tr1}\cos(\beta)$, $z_1=x_{Tr1}\sin(\beta)$ and $V_{Z1}=V_{Tr1}\sin(\beta)$. These relationships, combined with the similarity of the first two terms in Equations 18 and 19, mean that if the initial angles α_0 and β are randomly distributed then a circular dispersion pattern is to be expected, as observed by Tachikawa (1988).

The largest dispersion predicted by these equations occurs when α_0 is small, say 1°, which with the approximation that the mean drag coefficient $C_D = 0.6C_{N90}$ leads to $x_{Ax1}\approx 2L_X/9$, $x_{Tr1}\approx \pi L_X/6$ and $V_{Ax1}\approx V_{Tr1}\approx W(5BL_X/9)^{0.5}$ and hence

$$x \approx \frac{2L_X}{9} + W(t-t_1) - \frac{1}{B}\ln\left(1+BW\left(1-(5BL_X/9)^{0.5}\right)(t-t_1)\right) \tag{20}$$

$$y \approx \frac{\pi L_X \cos(\beta)}{6} + \cos(\beta)(5BL_X/9)^{0.5}\frac{\ln\left(1+BW\left(1-(5BL_X/9)^{0.5}\right)(t-t_1)\right)}{B\left(1-(5BL_X/9)^{0.5}\right)} \tag{21}$$

$$z \approx \frac{\pi L_X \sin(\beta)}{6} + \sin(\beta)(5BL_X/9)^{0.5}\frac{\ln\left(1+BW\left(1-(5BL_X/9)^{0.5}\right)(t-t_1)\right)}{B\left(1-(5BL_X/9)^{0.5}\right)} + gravity \quad term \tag{22}$$

4.3 *Example trajectories*

Figure 7 shows the horizontal velocities and displacements predicted, with W=30 m/s, α_0=1° and β=0°, for two sample pieces of debris. These are a 4 to 1 aspect ratio corrugated steel plate and a 4 kg 100 by 50 mm wooden rod (See Table 2 for details). The predicted displacement behaviour of the plate is similar to that seen in Figure1(b), although the value of only 12.7 m at 50 m range is somewhat smaller than might be expected from the numerical results discussed in Section 3, where the standard deviation was 9 m. This may be partially due to ignoring rotational damping, which could increase dispersion. Figure 7 also shows that the rod, with its lower ballistic coefficient, is slower to accelerate during the initial phase but then maintains that velocity for longer and hence still has a moderate displacement.

Table 2. Properties of two debris examples

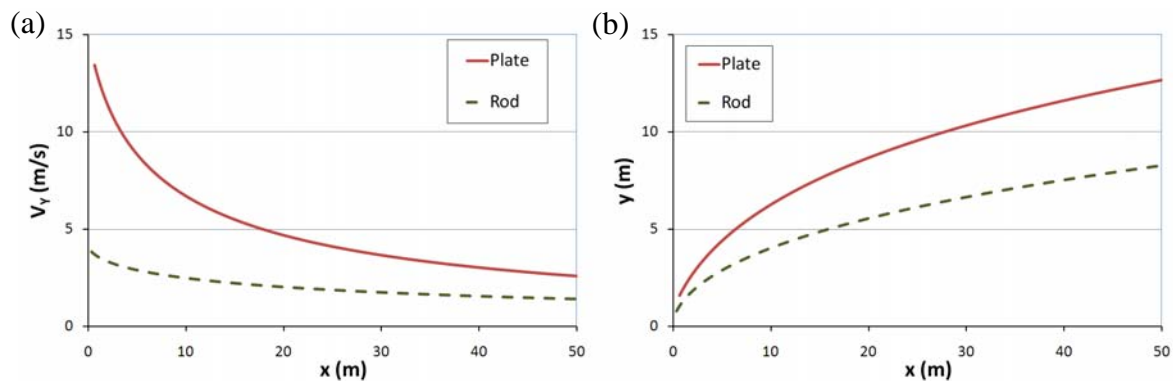| Material	Length (m)	Width (mm)	Thickness (mm)	Density (kg/m^3)	Mass (kg)	C_{N90}	C_D	B
Corrugated steel plate	3.0	750	0.45	8000	8.1	1.18	0.708	0.12
Timber rod	1.5	100	50	533	4.0	1.42	0.852	0.02

Figure 7. Horizontal (a) velocity and (b) displacement for a rod and plate in a 30m/s wind with α_0=1° and β=0°.

5 CONCLUSIONS

The dispersion of windborne debris can be divided into an initial rapid acceleration phase followed by a more gradual process where the trajectory can be modelled as that of a compact object. Solutions to the equations of motion have been proposed. A circular dispersion pattern and sensible displacements are predicted although there is room for improvement.

6 REFERENCES

Holmes J.D., 2004. Trajectories of spheres in strong winds with application to wind-borne debris, J. Wind Engineering and Industrial aerodynamics. 92, 9-22.

Holmes, J., Wehner, M., Sandland, C., Edwards, M., 2010. Modelling damage to residential buildings from wind-borne debris – Part 1, Methodology. 14th Australasian Wind Engineering Workshop, Canberra, 46-49.

Lin, N, Vanmarcke, E., 2010. Windborne debris risk analysis – Part I. Introduction and methodology, Wind and Structures, 13(2), 191-206.

Martinez-Vazquez, P., Baker, C.J., Sterling, M., Quinn, A., Richards, P.J., 2010. Aerodynamic forces on fixed and rotating plates, Journal of Wind and Structures, 13(2), 127-144, 2010.

Richards, P.J., Williams, N., Laing, B., McCarty, M., Pond, M., 2008. Numerical calculation of the 3-dimensional motion of wind-borne debris, J. Wind Engineering and Industrial aerodynamics, 96, 2188-2202.

Tachikawa, M., 1988. A method for estimating the distribution range of trajectories of wind-borne missiles, J. Wind Engineering and Industrial aerodynamics, 29, 175-184.

Wehner, M., Sandland, C., Holmes, J., Henderson, D., Edwards, M., 2010. Modelling damage to residential buildings from wind-borne debris – Part 2. Implementation. 14th AWES Workshop, Canberra, 50-53.

Wills, J.A.B., Lee, B.E. and Wyatt, T.A., 2002. A model of wind-borne debris damage. J. Wind Engineering and Industrial Aerodynamics, 90, 555 - 565.